

# Charge disproportionation and collinear magnetic order in the frustrated triangular antiferromagnet $\text{AgNiO}_2$

E. Wawrzyńska<sup>1</sup>, R. Coldea<sup>1</sup>, E.M. Wheeler<sup>2,3</sup>, T. Sörgel<sup>4</sup>, M. Jansen<sup>4</sup>, R.M. Ibberson<sup>5</sup>, P.G. Radaelli<sup>5,6</sup>, M.M. Koza<sup>3</sup>

<sup>1</sup>*H.H. Wills Physics Laboratory, University of Bristol,  
Tyndall Avenue, Bristol, BS8 1TL, United Kingdom*

<sup>2</sup>*Clarendon Laboratory, University of Oxford, Parks Road, Oxford OX1 3PU, United Kingdom*

<sup>3</sup>*Institut Laue-Langevin, BP 156, 38042 Grenoble Cedex 9, France*

<sup>4</sup>*Max-Planck Institut für Festkörperforschung, Heisenbergstrasse 1, D-70569 Stuttgart, Germany*

<sup>5</sup>*ISIS Facility, Rutherford Appleton Laboratory, Chilton, Didcot OX11 0QX, United Kingdom*

<sup>6</sup>*Dept. of Physics and Astronomy, University College London,  
Gower Street, London WC1E 6BT, United Kingdom*

(Dated: October 29, 2018)

We report a high-resolution neutron diffraction study of the crystal and magnetic structure of the orbitally-degenerate frustrated metallic magnet  $\text{AgNiO}_2$ . At high temperatures the structure is hexagonal with a single crystallographic Ni site, low-spin  $\text{Ni}^{3+}$  with spin-1/2 and two-fold orbital degeneracy, arranged in an antiferromagnetic triangular lattice with frustrated spin and orbital order. A structural transition occurs upon cooling below 365 K to a tripled hexagonal unit cell containing three crystallographically-distinct Ni sites with expanded and contracted  $\text{NiO}_6$  octahedra, naturally explained by spontaneous charge order on the Ni triangular layers. No Jahn-Teller distortions occur, suggesting that charge order occurs in order to lift the orbital degeneracy. Symmetry analysis of the inferred Ni charge order pattern and the observed oxygen displacement pattern suggests that the transition could be mediated by charge fluctuations at the Ni sites coupled to a soft oxygen optical phonon breathing mode. At low temperatures the electron-rich Ni sublattice (assigned to a valence close to  $\text{Ni}^{2+}$  with  $S = 1$ ) orders magnetically into a collinear stripe structure of ferromagnetic rows ordered antiferromagnetically in the triangular planes. We discuss the stability of this uncommon spin order pattern in the context of an easy-axis triangular antiferromagnet with additional weak second neighbor interactions and interlayer couplings.

PACS numbers: 75.25.+z, 71.45.Lr, 75.10.Jm, 75.40.Cx

## I. INTRODUCTION

Two-dimensional frustrated quantum magnets have attracted a wide interest theoretically<sup>1</sup> and experimentally<sup>2</sup> as possible candidates to display strong fluctuations that could potentially stabilize unconventional ordered phases,<sup>3</sup> spin-liquid<sup>4</sup>, or orbital-liquid<sup>5</sup> states. Low-spin triangular-lattice antiferromagnets are canonical frustrated models and the delafossite  $\text{AgNiO}_2$  with Ni ions arranged in well-separated triangular lattices has been proposed to show frustration effects both in the magnetic as well as in the orbital sector. Based on magnetic susceptibility measurements Shin et al.<sup>6</sup> proposed that Ni ions are in the low-spin configuration  $\text{Ni}^{3+}$  ( $t_{2g}^6 e_g^1$ ) with  $S=1/2$ , coupled by dominant in-plane frustrated antiferromagnetic interactions, and from x-ray measurements they proposed a high-symmetry crystal structure where each Ni ion has an unpaired electron in a doubly-degenerate  $e_g$  orbital. The cooperative orbital order is strongly frustrated because the orbital interactions have a strong bond-directional dependence<sup>7</sup> favoring different orbitals for pairs of Ni ions along the three different directions in the triangular lattice and this leads to a large manifold of degenerate mean-field states. The ground state in this spin-orbital problem is still highly debated theoretically with proposals ranging from orbital liquids to non-trivial forms of orbital order depending on fine details of the interactions.<sup>3,5,8</sup> Among

the experimentally explored candidate spin-1/2 materials to display this physics are  $\text{NaTiO}_2$  (non-magnetic after structural transition at low temperatures),<sup>9</sup>  $\text{NaNiO}_2$  (quasi-2D spin-1/2 ferromagnet with ferro-distortive orbital order)<sup>10</sup>, and  $\text{LiNiO}_2$  (no long-range magnetic or orbital order, but evidence for local Jahn-Teller distortions, difficulty in preparing pure stoichiometric samples).<sup>8</sup> The triangular magnet  $\text{AgNiO}_2$  and the two-silver-layer version  $\text{Ag}_2\text{NiO}_2$  (Refs. 11,12) are relatively unexplored experimentally and promise to be rather different from the above-mentioned systems as they both show dominant *antiferromagnetic* interactions,<sup>13</sup> thus potentially displaying frustrated magnetism.

$\text{AgNiO}_2$  is part of the large family of delafossite  $A^+M^{3+}\text{O}_2$  materials often studied as candidate two-dimensional frustrated magnets because the transition metal ion ( $M$ ) sits at the vertices of a triangular lattice in the basal plane, made up of a network of edge-sharing  $\text{MO}_6$  octahedra. Like most delafossites, it occurs in two structural polytypes which differ in the way the  $\text{NiO}_2$  layers are stacked along the  $c$ -axis: a 3-stage structure, where successive layers are in the same orientation but have an in-plane offset with Ni ions forming a 3-stage staircase along  $c$ -axis (3R polytype, rhombohedral space group  $R\bar{3}m$ , Refs. 6,14), or a 2-stage structure, where successive layers are stacked right on top of each other but are rotated by  $180^\circ$  (2H polytype, hexagonal space group  $P6_3/mmc$  shown in Fig. 1(a), Ref.

15). All measurements reported here have been made on the less-studied 2-stage polytype, the so called 2H-AgNiO<sub>2</sub>, recently synthesized using high-oxygen pressure techniques.<sup>15</sup> This polytype has metallic-like conductivity from 300 K down to low temperatures and the susceptibility indicates antiferromagnetic order near 20 K,<sup>15</sup> but the magnetic structure has not been determined up to now.

In the ideal crystal structure of both 3R and 2H polytypes of AgNiO<sub>2</sub> Ni ions have both spin and orbital degrees of freedom. The local crystal field is octahedral near-cubic and in the case of strong crystal field proposed herein<sup>6,15</sup> the electronic state of Ni<sup>3+</sup> ( $3d^7$ ) is the low-spin state  $t_{2g}^6 e_g^1$  with one unpaired electron (spin-1/2) in the upper  $e_g$  level. A small trigonal distortion present in the crystal structure due to squashing of the NiO<sub>6</sub> octahedra along the  $c$ -axis changes the detailed wavefunctions of the orbital states but does not lift the two-fold degeneracy of the upper  $e_g$  level because it preserves a local three-fold symmetry rotation axis along  $c$ . Each Ni ion has a tendency to locally distort the environment to lower its orbital energy due to the Jahn-Teller effect, however the cooperative orbital order on the triangular lattice is frustrated as the orbital exchange favors occupation of different orbitals for pairs of Ni ions along the three different in-plane directions. Such systems are susceptible to form an orbital liquid state at low temperatures or to have the orbital degeneracy lifted by structural distortions.

In measurements reported here we find evidence for a weak structural modulation in 2H-AgNiO<sub>2</sub> leading to a tripling of the unit cell in the hexagonal basal plane. This can be naturally explained by charge disproportionation on the Ni sites into three sublattices, which we propose occurs in order to lift the orbital degeneracy of the Ni<sup>3+</sup> ions. This physics is in sharp contrast to the insulator NaNiO<sub>2</sub> where the orbital degeneracy is lifted by Jahn-Teller orbital order leading to a monoclinic crystal structure.<sup>10</sup> We attribute this difference to the fact that 2H-AgNiO<sub>2</sub> being metallic charge transfer can be an energetically more favourable mechanism to lift the orbital degeneracy compared to local Jahn-Teller distortions found in more localized systems.

At low temperatures the electron-rich Ni sublattice (attributed to a valence close to Ni<sup>2+</sup> with spin  $S = 1$ ) orders magnetically in a collinear stripe structure with spins pointing along the  $c$ -axis and arranged in alternating ferromagnetic rows in the triangular plane. This magnetic structure cannot be explained at the mean-field level by a minimal spin model on a triangular lattice containing only nearest-neighbor antiferromagnetic exchange and easy-axis anisotropy, and we propose that it is stabilized by additional weak second neighbor antiferromagnetic in-plane interactions and/or weak ferromagnetic interlayer couplings.

The rest of the paper is organized as follows. Next Section (II) presents the experimental details of the neutron, X-ray, susceptibility and specific heat measurements.

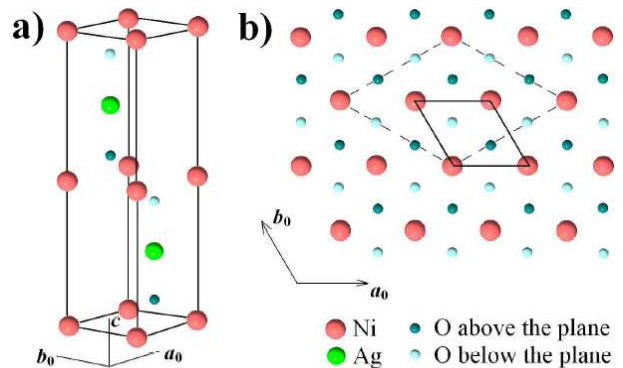


FIG. 1: (color online) Nominal crystal structure of 2H-AgNiO<sub>2</sub> deduced from X-ray measurements in Ref. 15 (space group  $P6_3/mmc-D_{6h}^4$ ). (a) There are two NiO<sub>2</sub> layers per unit cell related by a mirror plane reflection through the Ag<sup>+</sup> layer at  $z = 1/4$ . (b) Basal plane showing the triangular network of Ni ions (large red balls) coordinated by oxygens (small blue balls). Thick solid line contour shows the unit cell and dashed line shows the unit cell tripling in the distorted structure.

Diffraction measurements of the room-temperature crystal structure are presented and analyzed in Sec. III where a lower-symmetry space group is proposed to accommodate the observed structural modulation. A transition to the high-symmetry, undistorted crystal structure is observed upon heating to high temperatures and this is discussed in Sec. IV followed by a symmetry analysis of the structural distortion in terms of symmetry-allowed basis vectors in Sec. V. This is used to propose that the mechanism for the structural distortion is charge fluctuations at the Ni site coupled with a soft zone-boundary optical phonon involving oxygen breathing modes (further calculations using co-representation symmetry analysis to uniquely determine the distorted space group are presented in Appendix B). Susceptibility and specific heat measurements are shown in Sec. VI, followed by measurements of the magnetic structure analyzed in terms of symmetry-allowed basis vectors and discussed in terms of a minimal Hamiltonian containing exchange and easy-axis anisotropy (Sec. VII). Finally, the results are summarized and discussed in Sec. VIII. For completeness we include in Appendix A a list of the measured supercell and magnetic structure factors. A partial account of the results describing the room-temperature crystal structure and low-temperature magnetic order has been reported in ref. 16.

## II. EXPERIMENTAL DETAILS

Powder samples of the 2H-AgNiO<sub>2</sub> (< 1% admixture of the 3R polytype) were prepared from Ag<sub>2</sub>O and Ni(OH)<sub>2</sub> using high oxygen pressures (130 MPa) as de-

TABLE I: Lattice parameters and atomic positions in the unit cell in the ideal ( $P6_3/mmc$ ) and the distorted ( $P6_322$ ) structural space groups at 300 K. Oxygen positions are parameterized by an out-of-plane height  $z_O = 0.08050(5)$  and an in-plane displacement  $\epsilon = 0.0133(2)$ . The distorted unit cell is tripled in the hexagonal plane with an unchanged extent along the  $c$ -axis, but the origin is shifted by  $c/4$  such that the two  $NiO_2$  layers appear now at  $z = 1/4$  and  $3/4$ . Throughout this paper we use different symbols,  $a_0$  and  $a = \sqrt{3}a_0$ , to denote the hexagonal lattice parameter of the ideal and distorted structures, respectively.

$P6_3/mmc$ (no. 194)			$P6_322$ (no. 182)		
$a_0 = 2.93919(5) \text{ \AA}$			$a = 5.0908(1) \text{ \AA}$		
$c = 12.2498(1) \text{ \AA}$			$c = 12.2498(1) \text{ \AA}$		
Atom Site $(x, y, z)$			Atom Site $(x, y, z)$		
Ni	$2a$	$(0, 0, 0)$	Ni1	$2c$	$(\frac{1}{3}, \frac{2}{3}, \frac{1}{4})$
			Ni2	$2b$	$(0, 0, \frac{1}{4})$
			Ni3	$2d$	$(\frac{1}{3}, \frac{2}{3}, \frac{3}{4})$
Ag	$2c$	$(\frac{2}{3}, \frac{1}{3}, \frac{1}{4})$	Ag	$6g$	$(\frac{2}{3}, 0, 0)$
O	$4f$	$(\frac{2}{3}, \frac{1}{3}, z_O)$	O	$12i$	$(\frac{1}{3}, \epsilon, \frac{1}{4} + z_O)$

scribed in Ref. 15. Neutron diffraction patterns to probe the crystal and magnetic structure were collected using the high-resolution back-scattering time-of-flight diffractometers OSIRIS ( $0.65 < Q < 6 \text{ \AA}^{-1}$ ) and HRPD ( $2 < Q < 9 \text{ \AA}^{-1}$ ) at the ISIS Facility of the Rutherford Appleton Laboratory in the UK. Preliminary measurements were also performed using GEM at ISIS and the monochromatic neutron diffractometer D1B at the Institute Laue-Langevin in France. The magnetic order parameter was obtained from elastic neutron scattering measurements using the direct-geometry time-of-flight spectrometer IN6 and the temperature-dependence of the lattice constants was also measured on D2B, both at the ILL. X-ray powder diffraction measurements to help solve the crystal structure at room temperature were made using a Philips X’pert diffractometer ( $\lambda_{CuK\alpha} = 1.54 \text{ \AA}$ ). Structural and magnetic refinement was made using the FullProf programme.<sup>17</sup> Susceptibility measurements were made using a SQUID magnetometer (Quantum Design MPMS) and specific heat data was collected on a pressed powder pellet using a Quantum Design PPMS system.

### III. CRYSTAL STRUCTURE

The neutron powder diffraction pattern collected at room temperature ( $T=300 \text{ K}$ , Fig. 2) is overall in good agreement with the hexagonal space group  $P6_3/mmc$  proposed before.<sup>15</sup> However, a close inspection shows the presence of a number of additional low-intensity peaks (below 1% of the main peak) that could be indexed in this space group by *fractional* wavevectors such as  $(2/3, -1/3, 0)$  and  $(2/3, -1/3, 1)$  in Fig. 3(b), and such supercell peaks systematically accompany the main structural

peaks throughout the wide  $Q$ -range probed [see panel a)] and are displaced in  $Q$  following the lattice contraction upon cooling [see paired up-down panels b-c), e-f) and h-i)]. These extra peaks are naturally interpreted in terms of a structural modulation equivalent to a tripling of the unit cell in the basal plane. Complementary X-ray measurements [Fig. 3 d,g,j] did not show a measurable intensity at the supercell positions, suggesting that the structural modulation involves mainly displacements of the light oxygen ions which have a very small X-ray cross-section, as any significant displacements of the heavier Ag or Ni ions would have implied occurrence of supercell peaks not observed in the collected X-ray pattern. Therefore to model the distortion we refined only the oxygen positions and considered in order of decreasing symmetry all subgroups of the ideal structure ( $P6_3/mmc$ ) compatible with a tripling of the unit cell in the  $ab$  plane, i.e. a unit cell of size  $\sqrt{3}a_0 \times \sqrt{3}a_0 \times c$  (6 Ag, 6 Ni and 12 O atoms per unit cell). We eliminated the space groups that were not compatible with the observed low-temperature magnetic structure [see Sec. VII] where 2 Ni ions in the unit cell are magnetically ordered and 4 are unordered, i.e. we only considered the space groups where the magnetically-ordered and unordered Ni ions occupied distinct crystallographic sites. The highest symmetry subgroup in which both the structural and magnetic data could be described is  $P6_322$  (no. 182) where all 12 oxygen atoms are symmetry-related and compared to the ideal structure are displaced by a small amount  $\epsilon$  along one of the in-plane triangular directions. The observed supercell reflections could be well described by this model and the best fit to the data is shown in Figs. 2 and 3 (solid lines,  $R_{\text{Bragg}} = 5.55\%$ ,  $R_F = 6.49\%$ ) (structure factors are listed in Table. V in the Appendix A). The obtained lattice parameters and positions in the unit cell are listed in Table. I. As a further test we refined the lattice parameters using only the main peaks or only the supercell peaks and obtained similar values ( $a = 5.09082(1) \text{ \AA}$ ,  $c = 12.24984(4) \text{ \AA}$  and  $a = 5.0908(2) \text{ \AA}$ ,  $c = 12.250(2) \text{ \AA}$ , respectively) corroborating the fact that the weak supercell peaks belong to the same phase as the main peaks and are not due to an extra phase.

Fig. 4 shows a schematic diagram of the  $z = 1/4$   $NiO_2$  layer of the distorted structure. The distortion preserves the 3-fold rotation axis at each Ni site but the displacements of the oxygens lead to one Ni site with expanded Ni-O bonds (Ni1) and two other sites with contracted bonds (Ni2 and Ni3); the black circles centered on the Ni sites correspond to Ni-O distances of  $2.022 \text{ \AA}$  (Ni1) and  $1.934 \text{ \AA}$  (Ni2 and Ni3), respectively. In  $Ni^{2+}$  oxides<sup>18</sup> typical Ni-O bond distances are about  $\sim 2.09 \text{ \AA}$ , whereas in  $Ni^{4+}$  oxides<sup>19</sup> they decrease to  $1.92 \text{ \AA}$ . This comparison suggests a charge disproportionation among the Ni sites on the triangular layers in  $2H\text{-AgNiO}_2$  between electron-rich Ni1 sites (expanded  $NiO_6$  octahedron) with valence close to  $Ni^{2+}$  and electron-depleted sites Ni2 and Ni3 (contracted octahedra) close to  $Ni^{3.5+}$  (to ensure charge neutrality). Using a phenomenological

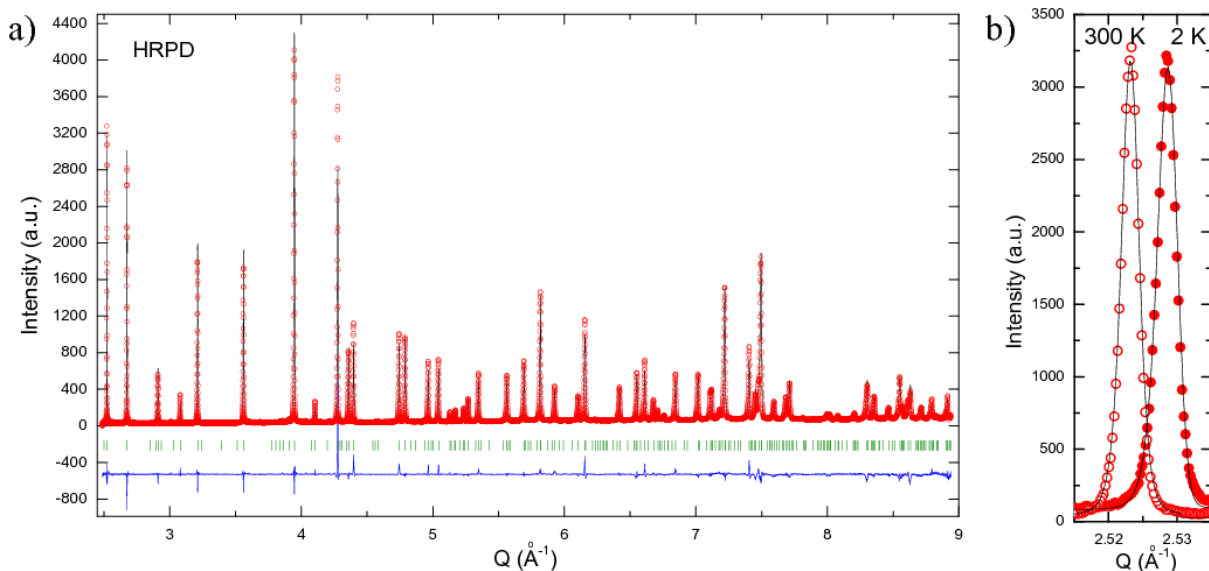


FIG. 2: (color online) (a) Room temperature (300 K) neutron diffraction pattern obtained using HRPD (resolution  $\Delta Q/Q \sim 10^{-3}$ , 15 hours counting on an 11 g powder sample). The solid curve through data points is a fit to the distorted  $P6_322$  space group. Vertical bars indicate Bragg peak positions and the bottom curve shows the difference between the fit and the data. Zoomed-in regions showing weak supercell peaks are plotted in Fig. 3. (b) Detail of the (111) peak lineshape expected to split in the case of a structural distortion to an orthorhombic or monoclinic structure. No splitting could be detected, and the lineshape at both 300 K (open symbols) and 2 K (filled circles) could be well described by a resolution-convolved profile for the hexagonal  $P6_322$  space group (solid lines) with lattice parameters adjusted for thermal contraction upon cooling.

bond-valence model<sup>20</sup> to relate the valence of the central ion to the bond-lengths,  $v = \sum_i e^{(r_0 - r_i)/B}$  where  $B=0.37 \text{ \AA}$  and  $r_0 = 1.686 \text{ \AA}$  for the  $\text{Ni}^{3+}\text{-O}^{2-}$  pair, gives nominal valences in the ionic limit for the three sites as 2.42 (Ni1) and 3.07 (Ni2 and Ni3), suggesting a significant, but most likely only partial charge disproportionation. We note that the bond lengths found in  $2\text{H-AgNiO}_2$  are similar to those found in  $\text{YNiO}_3$  [ $d(\text{Ni1-O})=1.923 \text{ \AA}$  and  $d(\text{Ni2-O})=1.994 \text{ \AA}$ , ref. 21], proposed to have a charge disproportionation into two Ni sublattices of valences  $\text{Ni}^{3\pm\sigma}$  ( $\sigma \simeq 0.35$ ).

Upon cooling to lower temperatures no evidence for a further structural distortion could be found. At 2 K the main and supercell peaks are displaced in wavevector following the lattice contraction and the structural peaks could be well described [see solid lines in Fig. 3 c,f,i)] by the same crystal structure as at 300 K but with shorter lattice parameters  $a = 5.08110(2) \text{ \AA}$  and  $c = 12.24670(7) \text{ \AA}$  ( $R_{\text{Bragg}} = 4.45\%$ ,  $R_{\text{F}} = 5.53\%$ ). We note that the related triangular-lattice material  $\text{NaNiO}_2$  behaves very differently showing a strong ferro-distortive transition into a low-temperature monoclinic structure with a significant difference (4%) in the two in-plane lattice parameters.<sup>10</sup> We tested for such a scenario in the  $2\text{H-AgNiO}_2$  where a departure from hexagonal symmetry could be accommodated within the orthorhombic  $Cmcm$  space group with lattice parameters  $a \times b \times c$ . Within the experimental accuracy no splitting of the main peaks could be detected [see Fig. 2b)] and the fitted in-plane lat-

tice parameters had the same ratio as in the undistorted structure ( $b/a = \sqrt{3}$ ) to within better than 0.02%, so we concluded that the hexagonal symmetry is preserved down to the lowest temperature probed of 2 K.

#### IV. TRANSITION TO THE HIGH-SYMMETRY STRUCTURE AT HIGH TEMPERATURES

We also measured the diffraction pattern at high temperatures motivated by recent resistivity measurements<sup>12</sup> reporting a weak anomaly near 365 K, proposed to originate from a structural transition. We observed that upon heating the triple-cell peaks decreased in intensity and could not be observed above  $T_S = 365(3) \text{ K}$ , which coincides with the location of the transport anomaly. Fig. 5(a) shows that triple-cell peaks are absent in the 420 K data and the main structural peaks are only slightly displaced in  $Q$  due to lattice expansion. The collected diffraction patterns at various temperatures were refined in the distorted space group  $P6_322$  and the obtained temperature-dependence of the oxygen displacement  $\epsilon$  away from the high-symmetry position is plotted in Fig. 5(b) inset and shows a rather rapid decrease near  $T_S$ . The lattice parameters increase smoothly with increasing temperature with no clear anomalies near the transition apart from possibly a small kink in the  $c$  lattice constant as linear fits to the data below and above 365 K (solid and dashed lines in Fig. 5(b)) give a slightly smaller slope

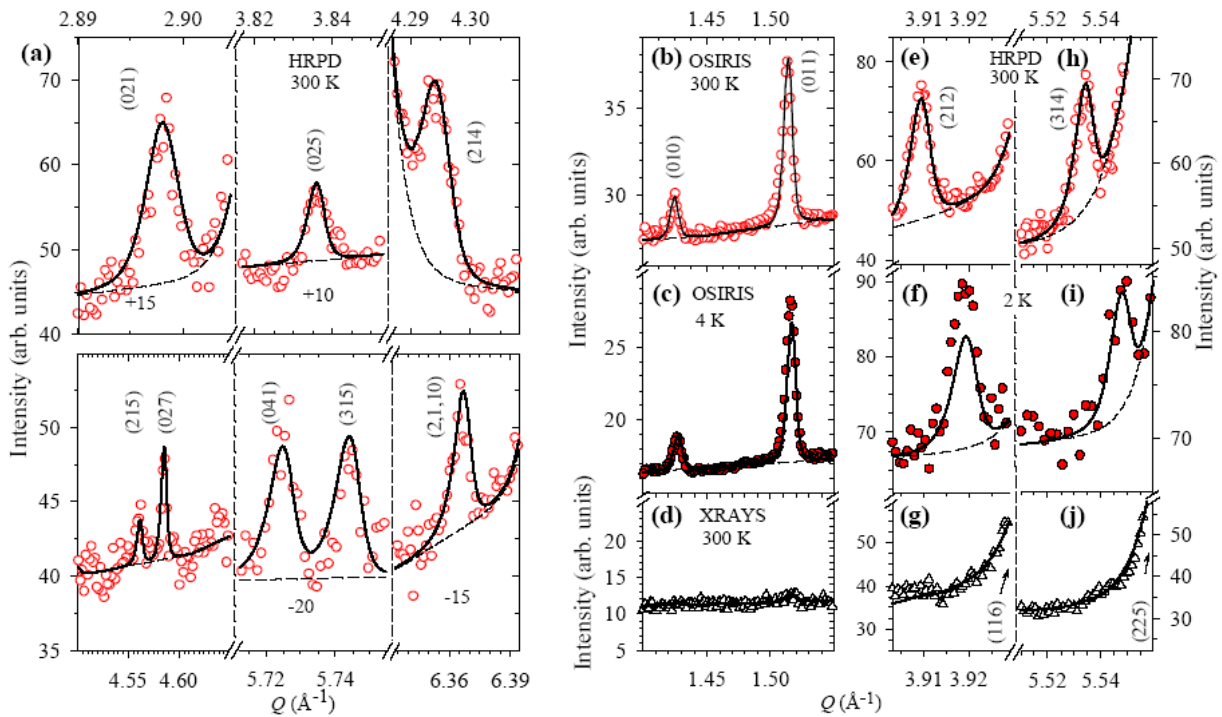


FIG. 3: Zoomed-in regions of the 300 K neutron diffraction pattern a),b),e),h) showing a number of the weak supercell reflections disallowed in the ideal  $P6_3/mmc$  structure and associated with a tripling of the unit cell in the  $ab$  plane. Solid lines are the calculated profile for the distorted  $P6_322$  structure in Fig. 4 and dashed lines show the estimated local background including the resolution tails of nearby main structural peaks (data in some subpanels is shifted vertically by indicated amounts for clarity). Paired panels b-c),e-f), h-i) show how the supercell peaks are displaced in  $Q$  following the lattice contraction upon cooling (the base temperature data has a higher overall background as it was collected in a cryostat). Supercell peaks are not observed in the X-ray data in bottom panels d,g,j), consistent with the structural modulation involving mainly displacements of the light oxygen ions.

in the low-temperature phase, consistent with the structural distortion in this phase making the crystal lattice more rigid so less able to expand upon increasing temperature. The disappearance of the supercell peaks at high temperature indicates a transition to the high-symmetry crystal structure where all Ni-O bonds become equivalent and charge is uniformly distributed on all Ni sites. Indeed the 420 K data could be well described by the undistorted  $P6_3/mmc$  space group with  $a_0 = 2.94267(3)$  Å,  $c = 12.2554(2)$  Å and oxygen height  $z_O = 0.07991(6)$  ( $R_{\text{Bragg}} = 11.8\%$ ,  $R_F = 7.13\%$ ).

To conclude the analysis of the diffraction pattern we note that in addition to the triple cell peaks identified above, the data also showed diffraction peaks due to a small admixture (1%) of the rhombohedral 3R polytype (currently at the limit at which pure hexagonal 2H polytype can be chemically prepared) and some other small peaks that could not be indexed by any obvious commensurate fractional index of the main peaks and which were still present at high temperatures above the structural transition at 365 K. Those were attributed to unidentified impurity phases below the 1% level that occurred during chemical synthesis (scanning electron microscopy (SEM) coupled with energy-dispersive X-ray analysis (EDX) of a

TABLE II: Basis vectors for the irreducible representations for charge (scalar) order at the Ni sites ( $2a$ ) in space group  $P6_3/mmc$  (no. 194) for propagation vector  $\mathbf{q}_0 = (1/3, 1/3, 0)$  obtained using group theory<sup>22</sup>.

position	$(0, 0, 0)$	$(0, 0, \frac{1}{2})$
$\Gamma_1$	1	1
$\Gamma_2$	1	-1

small part of the sample indicated small traces of Au, Al and Si, but the chemical composition could not be precisely identified). The alternative origin of those small peaks could have been instrumental (e.g. spurious sample holder reflections).

## V. SYMMETRY ANALYSIS OF THE STRUCTURAL DISTORTION

To understand better the mechanism of the structural transition at  $T_S = 365$  K from the ideal to the distorted structure we performed an analysis of

TABLE III: Basis vectors of the irreducible representations for displacement (polar vector) order at the oxygen sites (4f) in space group  $P6_3/mmc$  (no. 194) for propagation vector  $\mathbf{q}_0 = (1/3, 1/3, 0)$  obtained using group theory<sup>22</sup>.

position	$(\frac{2}{3}, \frac{1}{3}, z_O)$	$(\frac{1}{3}, \frac{2}{3}, 1-z_O)$	$(\frac{2}{3}, \frac{1}{3}, \frac{1}{2} - z_O)$	$(\frac{1}{3}, \frac{2}{3}, \frac{1}{2} + z_O)$
$\Gamma_1$	$(e^{i\pi/6}, e^{i\pi/2}, 0)$	$(e^{i\pi/2}, e^{i\pi/6}, 0)$	$(e^{i\pi/6}, e^{i\pi/2}, 0)$	$(e^{i\pi/2}, e^{i\pi/6}, 0)$
$\Gamma_2$	$(e^{i\pi/6}, e^{i\pi/2}, 0)$	$(e^{i\pi/2}, e^{i\pi/6}, 0)$	$-(e^{i\pi/6}, e^{i\pi/2}, 0)$	$-(e^{i\pi/2}, e^{i\pi/6}, 0)$

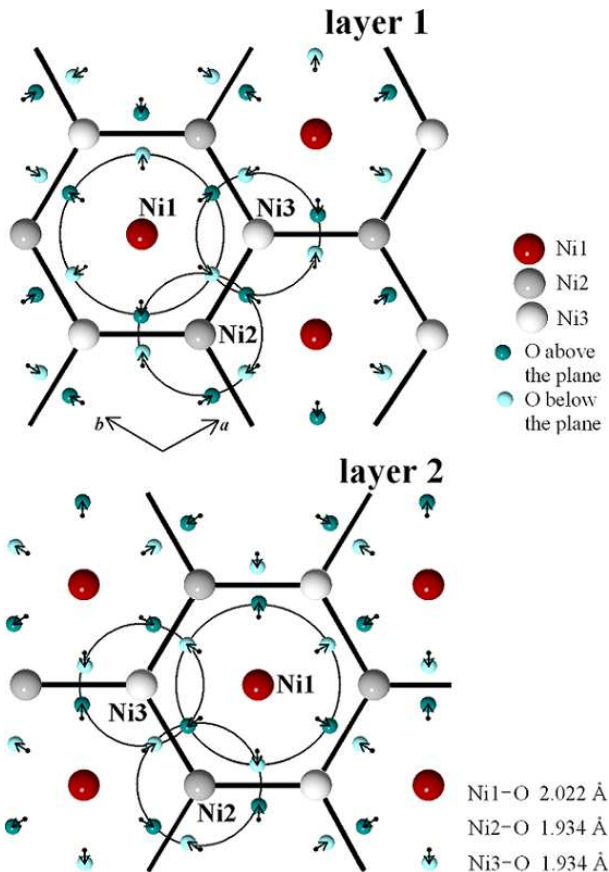


FIG. 4: (color online) (top) Schematic diagram of the  $\text{NiO}_2$  layer at  $z = \frac{1}{4}$  showing how the displacements (small arrows) of the oxygen ions (small balls) lead to a periodic arrangement of expanded (large circle, Ni1) and contracted (small circles, Ni2,3)  $\text{NiO}_6$  octahedra. Thick hexagonal contour shows the honeycomb network of contracted sites. The origin of the coordinate system is at the circled Ni2 site. (bottom) The expanded site Ni1 has a staggered zig-zag arrangement between even and odd layers stacked along the  $c$ -axis. Layer 2 in the unit cell ( $z = \frac{3}{4}$  and  $-\frac{1}{4}$ ) is obtained from layer 1 by 180° rotation around the central  $(\frac{1}{2}, \frac{1}{2}, z)$  axis followed by a  $c/2$  translation.

symmetry-allowed order patterns in the undistorted, high-temperature space group  $P6_3/mmc$  with the observed ordering wavevector  $\mathbf{q}_0 = (1/3, 1/3, 0)$ . We considered both the charge (scalar) order on the Ni sites as well as the oxygen ion displacements (polar vector order).

Our refined model for the structure in the distorted

phase in Fig. 4 shows a periodic arrangement of expanded (Ni1)  $\text{Ni}^{3-\sigma}$  and contracted (Ni2 and Ni3)  $\text{Ni}^{3+0.5\sigma}$  sites with  $\sigma = 1$  in case of complete charge disproportionation. To try to reproduce this we looked for symmetry-allowed charge (scalar) order patterns with propagation vector  $\mathbf{q}_0 = (1/3, 1/3, 0)$  at the Ni 2a sites (2 atoms) in the unit cell of the  $P6_3/mmc$  space group. The obtained irreducible representations and basis vectors are listed in Table II. There are two basis vectors ( $\tau_{1,2}$  corresponding to irreducible representations  $\Gamma_{1,2}$  in Table II) which physically correspond to having the same or opposite charges for Ni sites above each other in the two layers. The order pattern implied by the structural refinement cannot be described by a single basis vector, but can be described by a linear combination of two basis vectors, i.e.

$$\zeta = e^{i\pi/3} \left[ (\tau_1 + \tau_2) + e^{i4\pi/3} (\tau_1 - \tau_2) \right], \quad (1)$$

where  $\tau_i(1)$  is the charge on atom 1 (layer 1) for the basis vector  $\tau_i$  etc.

The corresponding charge order pattern (relative to the uniform high-temperature phase where each Ni site has valence +3) is shown in Fig. 6 and consists of a triangular lattice of charges  $-\sigma$ , i.e. electron-rich  $\text{Ni}^{3-\sigma}$ , surrounded by a honeycomb network of charges  $+0.5\sigma$ , i.e.  $\text{Ni}^{3+0.5\sigma}$ . This charge order pattern is obtained from the basis vector  $\zeta$  modulated by the phase factor due to the propagation vector  $\mathbf{q}_0$ , i.e. in the unit cell at distance  $\mathbf{r} = n_1\mathbf{a}_0 + n_2\mathbf{b}_0 + n_3\mathbf{c}$  from the origin ( $n_{1,2,3}$  integers) the charges are given by the real part of the complex vector

$$\tilde{Q}_{\mathbf{r}} = \frac{\sigma}{2} e^{i\mathbf{q}_0 \cdot \mathbf{r}} \zeta. \quad (2)$$

For atom 1 (layer 1) the charge is

$$Q_{\mathbf{r}}(1) = \sigma \cos(\mathbf{q}_0 \cdot \mathbf{r} + \pi/3) \quad (3)$$

and for atom 2 (layer 2) is

$$Q_{\mathbf{r}}(2) = \sigma \cos(\mathbf{q}_0 \cdot \mathbf{r} + 5\pi/3). \quad (4)$$

The normalization prefactor in eq. (2) gives the magnitude of the charge order and was chosen such as to obtain charge  $-\sigma$  on the Ni1 sites.

Subsequently we looked at possible order patterns for oxygen ion displacements corresponding to the same propagation wavevector  $\mathbf{q}_0$ . There are in total 4 one-dimensional and 2 two-dimensional irreducible representations that could describe displacement (polar vector)

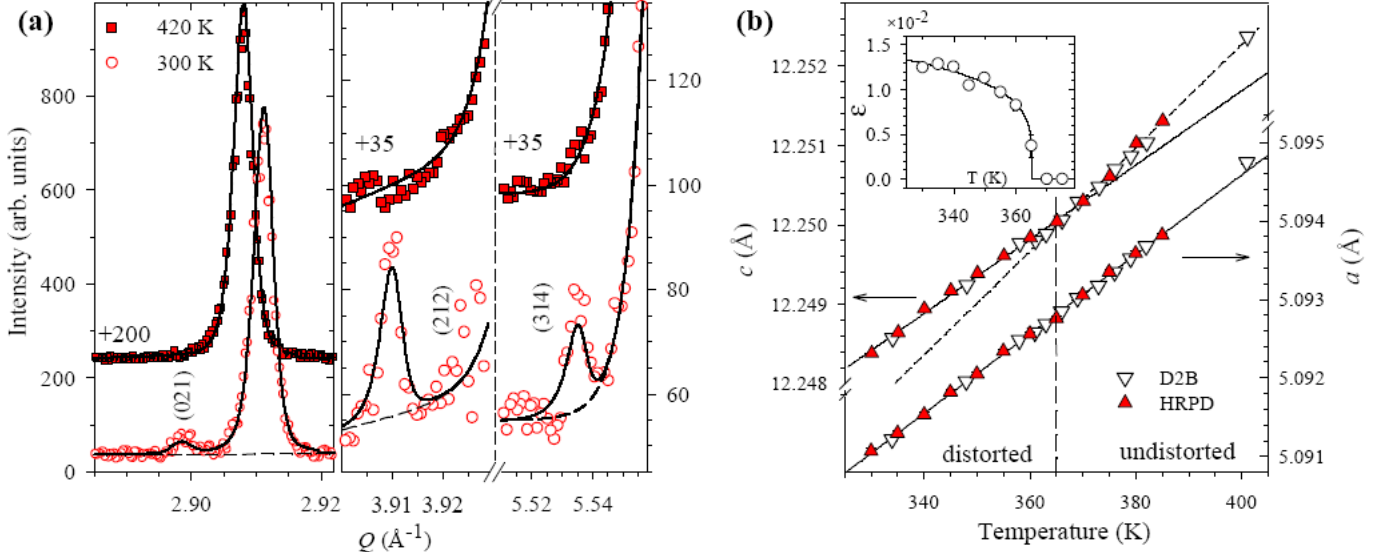


FIG. 5: (a) Comparison between 300 K (open symbols, lower trace) and 420 K data (filled symbols, upper trace) showing the absence of the triple-cell peaks (021), (212) and (314) at high temperature. Solid lines are fits to the distorted (300 K) and ideal structure (420 K), respectively and dashed lines show the estimated background level. The high-temperature data has been shifted vertically by the indicated offsets for clarity. (b) Temperature dependence of the lattice parameters:  $c$  left axis,  $a$  right axis. Solid (dashed) lines for the  $c$  parameter are straight line fits to the data below (above)  $T_S = 365$  K. Filled/open symbols are data from different instruments. Inset: temperature-dependence of the oxygen displacement parameter  $\epsilon$ , solid line is guide to the eye.

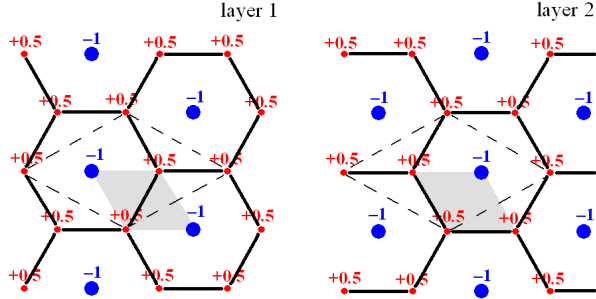


FIG. 6: (color online) Charge order pattern described by eq. (2) to be compared with Fig. 4. Labels -1 and +0.5 indicate charges in units of  $\sigma$ . Thick hexagonal contours indicate the honeycomb network of the electron depleted Ni<sub>2,3</sub> sites and dashed line contour is the unit cell of the charge-ordered structure. Light shaded area is the unit cell of the ideal structure with all Ni sites equivalent.

order at the  $4f$  oxygen sites (4 atoms per unit cell) and the two one-dimensional representations relevant for our discussion are listed in Table III. Basis vectors of these representations transform in the same way under the symmetry operations of the  $P6_3/mmc$  space group as the basis vectors for charge order listed in Table II so we use the same symbols  $\tau_1$  and  $\tau_2$ . Here they have complex components indicating a degeneracy with respect to rotation of the displacement vector in the  $ab$  plane. We again find that the observed structural displacements cannot be

described by a single basis vector, but is described by a linear combination of two basis vectors, i.e.

$$\xi = \frac{1}{2} e^{i7\pi/6} \left[ (\tau_1 + \tau_2) + e^{i4\pi/3} (\tau_1 - \tau_2) \right], \quad (5)$$

where the complex phase factor in front serves to rotate the oxygen displacement vector in the  $ab$  plane and with the chosen phase the displacement pattern is as in Fig. 4, i.e. oxygens displaced radially out of the expanded Ni sites (the numerical prefactor is used for normalization). In the above equation  $\tau_i(1)$  is the complex displacement vector for atom 1 in the representation  $\tau_i$  as per Table III. (Note that we use bold symbols to indicate vectors with components along the three crystallographic directions). The relative phase factor of the  $\tau_1$  and  $\tau_2$  basis vectors is the same for the polar order of oxygen displacements eq. (5) and for the charge order on the Ni sites eq. (1) as expected if the structural transition was driven by charge fluctuations coupled to an oxygen phonon breathing mode. It is noteworthy that the obtained oxygen displacements are consistent with an optic phonon mode at the Brillouin zone corner point  $\mathbf{q}_0$  predicted by lattice dynamics calculations<sup>23</sup> for a structure identical to one undistorted NiO<sub>2</sub> layer. So our results provide support that it is this phonon mode (probably modified slightly due to couplings with the Ag layer above and below) that mediates the  $\sqrt{3} \times \sqrt{3}$  charge order in the triangular NiO<sub>2</sub> planes.

In appendix B we provide further symmetry analysis of the basis vector modes for the charge and displace-

ment orders using co-representation analysis and prove that they uniquely identify the distorted space group as P6<sub>3</sub>22.

To conclude this section for completeness we quote below the expressions for obtaining the individual atomic displacements starting from the basis vector mode  $\xi$ . The order pattern is given by  $\xi$  modulated by the phase factor due to the propagation vector  $\mathbf{q}_0$ , i.e.

$$\tilde{\mathbf{d}}_r = 2\epsilon e^{i\mathbf{q}_0 \cdot \mathbf{r}} \xi, \quad (6)$$

where  $\mathbf{r} = (n_1, n_2, n_3)$  defines the unit cell and  $\xi(1)$  is the basis vector for atom 1 etc. The scale prefactor  $2\epsilon$  was introduced such as to give the absolute magnitude of the final displacements  $\epsilon\sqrt{3}a_0$  as per Table I. The real part of the above equation gives the actual displacement vectors

$$2\epsilon (\cos(\mathbf{q}_0 \cdot \mathbf{r} + \phi_x), \cos(\mathbf{q}_0 \cdot \mathbf{r} + \phi_y), 0) \quad (7)$$

where the phases  $\phi_{x,y}$  are given by the basis vector for that atom  $\xi = (e^{i\phi_x}, e^{i\phi_y}, 0)$  using eq. (5) and Table III. For example for the oxygen atom 1 in the unit cell at the origin  $\mathbf{r} = (0, 0, 0)$  the displacement is

$$2\epsilon (\cos(4\pi/3), \cos(5\pi/3), 0) = \epsilon(-1, 1, 0). \quad (8)$$

## VI. SUSCEPTIBILITY AND SPECIFIC HEAT

Magnetic susceptibility measured on a small powder sample is shown in Fig. 7(a). The pronounced drop at low temperatures near 20 K [see inset] is attributed to the onset of magnetic order and at higher temperatures above  $\sim 70$  K the data can be well described by a local-moment Curie-Weiss form plus a small temperature-independent part  $\chi_0$ ,

$$\chi = \frac{C}{T - \theta} + \chi_0 \quad (9)$$

where  $C = 0.445(5)$  emu K/mole,  $\theta_{CW} = -107(2)$  K, and  $\chi_0 = 1.7(1) \times 10^{-4}$  emu/mole, similar to previous reports.<sup>15</sup> The large negative Curie-Weiss temperature shows dominant antiferromagnetic interactions. Magnetic order occurs only at significantly lower temperatures,  $\sim 20$  K, suggesting that fluctuations due the low-dimensionality (mainly in-plane interactions) and the frustrated triangular geometry are important in suppressing the magnetic ordering temperature.

The effective magnetic moment extracted from the Curie-Weiss fit is  $\mu_{\text{eff}} = 1.88 \mu_B$  per Ni ion, and this was used previously<sup>15</sup> as evidence that Ni sites were in the low-spin Ni<sup>3+</sup> state ( $t_{2g}^6 e_g^1$ ) with  $S = 1/2$  ( $\mu_{\text{eff}} = 1.73 \mu_B$  for  $g = 2$ ). However, a charge disproportionation scenario as suggested by our structural measurements could also lead to similar values of the effective moment. In the extreme case of complete charge disproportionation the Ni1 site is Ni<sup>2+</sup>  $t_{2g}^6 e_g^2$  with a large spin moment  $S = 1$ , whereas the other sites are Ni<sup>3.5+</sup> likely to have only a

very small spin moment as they are close to Ni<sup>4+</sup> with a filled  $t_{2g}^6$  level, which has  $S = 0$ . The average effective moment observed by high-temperature susceptibility considering only  $S = 1$  moments on the Ni1 sites would then be  $\mu_{\text{eff}} = 1.63 \mu_B$  (for  $g = 2$ ), which is only 6% lower than the value for  $S = 1/2$  at every site, and it is possible that including a more realistic scenario of partial charge disproportionation (more likely to be the case here) could bring this estimate closer to the experiment.

Finally, we plot in Fig. 7(b) specific heat measurements which observe a sharp lambda-like peak identified with the magnetic transition near 20 K. No other anomalies could be observed up to the highest temperature studied of 240 K, consistent with no additional (structural) transitions occurring in this temperature range.

## VII. MAGNETIC STRUCTURE

The magnetic susceptibility shown in Fig. 7 (a) inset has a sharp downturn below 20 K as characteristic of a transition to antiferromagnetic order and below this temperature additional reflections are observed in the neutron diffraction pattern at low  $Q$ . The magnetic order peaks are most easily seen in the difference pattern 4 K – 300 K shown in Fig. 8 and can be indexed with respect to the P6<sub>3</sub>22 supercell by the commensurate propagation vector  $\mathbf{k} = (1/2, 0, 0)$ . The magnetic order parameter curves are plotted in Fig. 9 as a function of reduced temperature  $T/T_N$ . The Néel temperature obtained from the neutron data is 23.7(3) K is slightly higher than the location of the specific heat anomaly near 19.7(3) K, and susceptibility maximum near 21(1) K. This is probably due to a small temperature calibration offset in the neutron measurement where the sensor was at some distance away from the sample. We regard the absolute value of the transition temperature observed by the specific heat measurement  $T_N = 19.7(3)$  K as the most accurate, in agreement with recent  $\mu$ SR results.<sup>24</sup>

To find the magnetic structure we first consider in Table IV the magnetic basis vectors compatible with the symmetry of the P6<sub>3</sub>22 crystal structure for the six Ni ions in the unit cell (three sublattices). Symmetry constrains the moments on the same sublattice to be either parallel or antiparallel between the two layers in the unit cell. The best fit to the observed diffraction pattern (varying the spin direction and magnitude independently on the three sublattices) was obtained for the case when only one of the three sublattices was ordered, either Ni1 or Ni3, with a moment of 1.552(7)  $\mu_B$  along the  $c$ -axis and spins parallel between adjacent layers (irreducible representation  $\Lambda_3$  in Table IV with  $v \neq 0$  or  $v'' \neq 0$  and all the other spin components equal to 0). This correlates well with the structural analysis whereby the Ni1 site should have a large spin moment ( $S = 1$  at complete charge disproportionation Ni<sup>2+</sup>) whereas the other two sites (Ni2 and Ni3) with valences close to Ni<sup>3.5+</sup> would have a much smaller moment, as their configuration would be close to



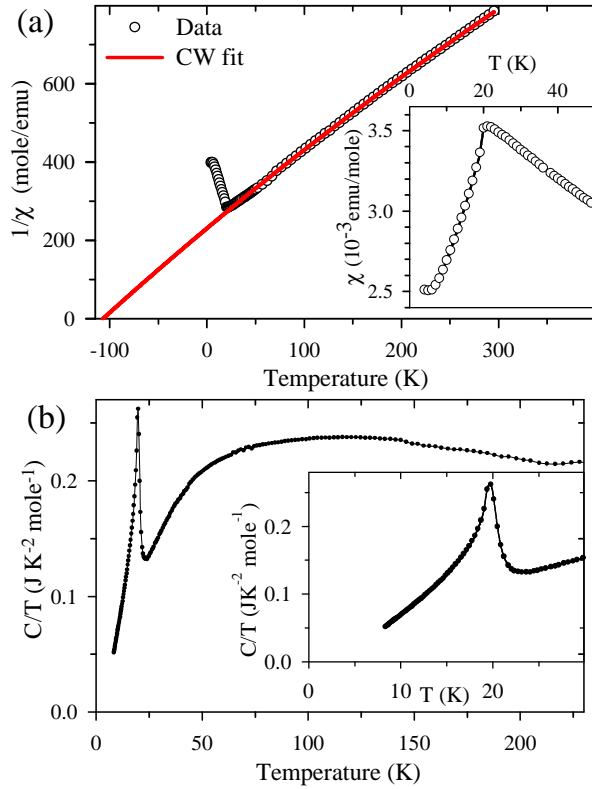


FIG. 7: (a) Inverse magnetic susceptibility ( $1/\chi$ ) fitted to a Curie-Weiss law eq. (1) (solid line) gives a large negative intercept indicating dominant antiferromagnetic interactions. Inset shows suppression of susceptibility below 20 K attributed to onset of antiferromagnetic order. (b) Temperature dependence of the specific heat observing a sharp lambda-like peak near the magnetic transition temperature.

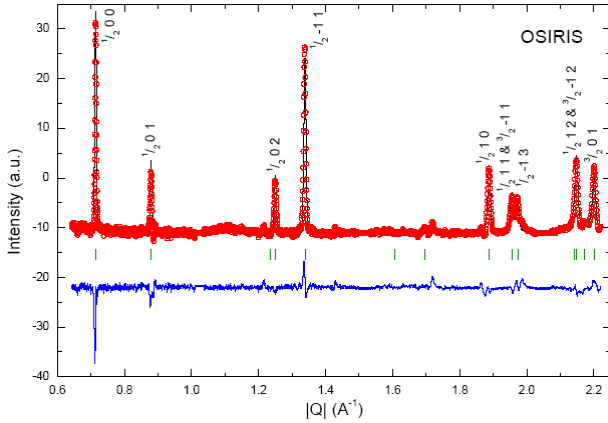


FIG. 8: Difference pattern 4 K – 300 K from OSIRIS showing peaks of magnetic origin, indexed by the propagation vector  $\mathbf{k}=(1/2,0,0)$ . The circles represent the observed intensities, the solid curve is a fit to the magnetic structure depicted in Fig. 10 and vertical bars indicate the magnetic Bragg peak positions. The bottom curve shows the difference between the fit and the data.

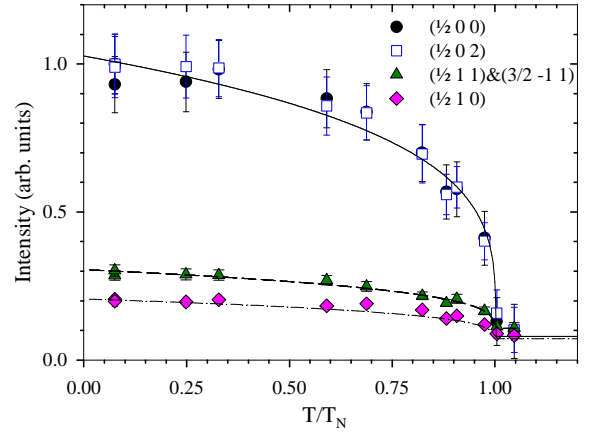


FIG. 9: Observed intensity of several magnetic Bragg peaks as a function of reduced temperature  $T/T_N$ . Data points are from elastic neutron powder scattering measurements using IN6. Lines are guides to the eye.

$\text{Ni}^{4+}$  with  $S = 0$ . Therefore we associate the magnetic order with site Ni1 carrying the largest spin moment.

The experimental data doesn't preclude the possibility of having also a very small magnetic moment along the  $c$ -axis on either Ni2 or Ni3 sites, these however could only be of the order of  $0.1 \mu_B$  at maximum (the spin arrangement would then be described by  $\Lambda_3$  with  $v'$  or  $v''$  equal to  $-0.1 \mu_B$ , respectively). Because taking into account these small magnetic moments doesn't improve the quality of fit in the following we assume for simplicity that only the sublattice Ni1 is ordered with a large spin moment.

The magnetic structure is illustrated in Fig. 10(a) and consists of alternating ferromagnetic stripes, i.e. spins are parallel along one of the three directions in the triangular plane and antiparallel along the other two directions. This structure can occur in three different domains obtained by  $\pm 60^\circ$  rotation around the  $c$ -axis, which would correspond to the symmetry-equivalent wavevectors  $\mathbf{k}'=(0,1/2,0)$  and  $\mathbf{k}''=(1/2,-1/2,0)$  of the star of  $\mathbf{k}$ . We note that the magnetic structure has only a 2-fold symmetry rotation axis along the  $c$ -axis whereas the crystal structure has 3-fold rotation symmetry along the  $c$ -axis. Three equal-weighted domains of those three structures would be expected in a macroscopic sample and each domain has the same powder-averaged diffraction pattern.

In the following we discuss possible mechanisms to stabilize the observed magnetic structure in a model of stacked triangular layers, so we consider the Hamiltonian

$$\mathcal{H} = \sum_{\text{NN}} J \mathbf{S}_i \cdot \mathbf{S}_j + \sum_{\text{NNN}} J' \mathbf{S}_i \cdot \mathbf{S}_k + \sum_{\text{interlayer}} J'' \mathbf{S}_i \cdot \mathbf{S}_l - D \sum_i (S_i^z)^2. \quad (10)$$

Here NN indicates summing over all in-plane nearest-neighbor pairs with coupling  $J$ , NNN denotes next-nearest-neighbour in-plane pairs with coupling  $J'$  [see

Fig. 10(b)] and  $J''$  is the inter-layer coupling (3 neighbors above and 3 below, see Fig. 10(a)), with  $J, J' > 0$  (antiferromagnetic) and  $J'' < 0$  (ferromagnetic). The last term in eq. (10) is an on site easy-axis anisotropy proposed to arise from crystal-field effects and required to stabilize the ordering spin direction along the crystallographic  $c$ -axis.

Considering first the 2D antiferromagnetic Heisenberg model ( $D = J'' = 0$  in eq. (10)) the ground state for NN couplings only is the 3-sublattice  $120^\circ$  spiral, however adding moderate antiferromagnetic NNN couplings  $1/8 \lesssim J'/J \leq 1$  stabilizes the collinear stripe order.<sup>25</sup> In fact for this model at the classical level the two-sublattice stripe order is degenerate with a continuous manifold of 4-sublattice non-collinear states but zero-point quantum fluctuations are predicted to lift this degeneracy through “order by disorder” and select the stripe ground state. An easy axis anisotropy  $D > 0$  is expected to further stabilize the collinear state thereby reducing the minimal required  $J'$ . At the classical level in the limit of very large anisotropy approaching the Ising limit the required  $J'$  becomes infinitesimally small, but is non zero.<sup>26</sup> In particular the NNN couplings are required to lift the degeneracy between the stripe state and the collinear state with 2 spins up and one down for each triangle, the so-called up-up-down state (UUD), with the ground state energy per spin  $e^S = (-J - J')S^2$  lower than  $e^{UUD} = (-J + 3J')S^2$  for antiferromagnetic  $J'$ . As an alternative to NNN couplings we note that the interlayer interactions could also provide a mechanism to lift this degeneracy as the stacking of magnetic layers energetically favors the stripe order. The interlayer energy is  $J''S^2$  (energy gain for  $J'' < 0$  ferromagnetic) for the stacked stripe order depicted in Fig. 10(a) where each spin has 4 favorable and 2 unfavorable interlayer bonds, whereas for a stacked UUD structure the interlayer energy is reduced to  $J''S^2/3$  because only  $2/3^{\text{rds}}$  of sites have 2 net favorable bonds and the remaining  $1/3^{\text{rd}}$  have 2 net unfavorable interlayer bonds. From this we conclude that the observed magnetic structure could be explained starting from an easy-axis nearest-neighbor triangular antiferromagnet with additional weak in-plane second neighbor antiferromagnetic exchange or weak ferromagnetic interlayer couplings.

## VIII. DISCUSSION AND CONCLUSIONS

To summarize, we have reported high-resolution neutron powder diffraction measurements in the orbitally-degenerate frustrated triangular magnet  $2\text{H-AgNiO}_2$ . We have observed a set of weak structural reflections, undetected in previous x-ray measurements, which indicate a small structural distortion with a tripling of the unit cell in the hexagonal basal plane. We have proposed that this could be explained by a periodic contraction and expansion of  $\text{NiO}_6$  octahedra in a three-sublattice structure as a consequence of charge disproportionation on the Ni

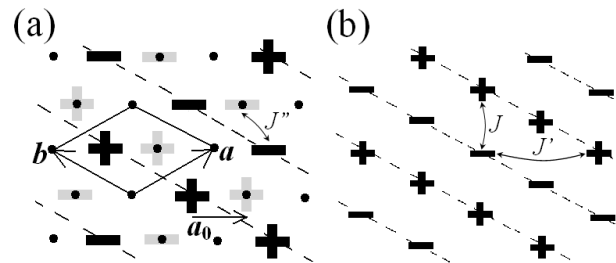


FIG. 10: (a) Magnetic structure of the Ni1 sublattice consisting of alternating rows (dashed lines) of ferromagnetically aligned spins.  $\pm$  symbols indicate the projection of the spin moment along the  $c$ -axis, dots represent the unordered (Ni2 and Ni3) Ni sites in the unit cell (solid contour). Thick black symbols indicate the moments in the bottom  $\text{NiO}_2$  plane ( $z = \frac{1}{4}$ ) whereas faint grey symbols correspond to the moments in the upper plane ( $z = \frac{3}{4}$ ) obtained by shifting the pattern by an in-plane offset  $\mathbf{a}_0$ . The arrowed line labelled  $J''$  indicates one of the three inter-layer exchange paths. The drawn structure has propagation vector  $\mathbf{k} = (1/2, 0, 0)$  (Bragg peaks indicated by black stars in Fig. 11), equivalent structures are obtained by  $\pm 60^\circ$  rotation around the  $(\frac{2}{3}, \frac{1}{3}, z)$ -axis. (b) In a single layer the ordered sites form a triangular lattice of spacing  $a$ . Short and long arrowed lines indicate the nearest- and next-nearest-neighbour exchanges  $J$  and  $J'$  in a minimal model proposed to explain the stability of the observed structure.

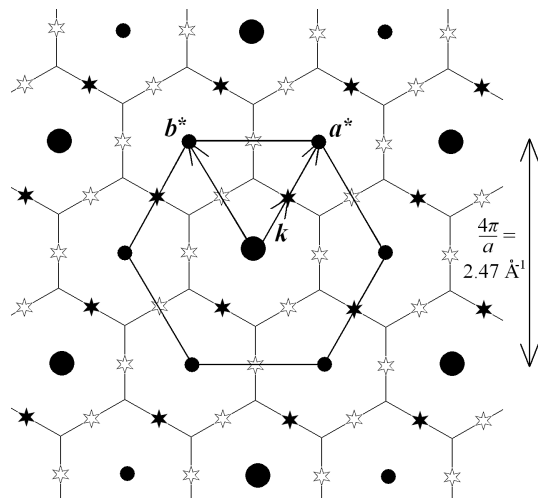


FIG. 11: Reciprocal basal plane showing locations of structural (filled circles) and magnetic reflections (stars). Large filled circles and large bold hexagon indicate the zone centers and Brillouin zone of the ideal, undistorted structure ( $P6_3/mmc$ ), whereas small filled circles and thin line hexagons are respectively structural supercell peaks and the Brillouin zone of the distorted crystal structure ( $P6_322$ ). Filled stars are the magnetic Bragg peak positions from the magnetic structure with propagation wavevector  $\mathbf{k} = (1/2, 0, 0)$  shown in Fig. 10, open stars are peaks from domains rotated by  $\pm 60^\circ$ .

TABLE IV: Basis vectors for irreducible representations for magnetic order at the six Ni ions in the unit cell (3 independent sublattices) for a structure with propagation vector  $\mathbf{k}=(1/2,0,0)$  for the  $P6_322$  space group obtained using group theory (MODY package<sup>22</sup>).  $u, v, u', v', u''$  and  $v''$  are independent spin components.

site	Ni1 (2c)		Ni2 (2b)		Ni3 (2d)	
position	$(\frac{1}{3}, \frac{2}{3}, \frac{1}{4})$	$(\frac{2}{3}, \frac{1}{3}, \frac{3}{4})$	$(0, 0, \frac{1}{4})$	$(0, 0, \frac{3}{4})$	$(\frac{1}{3}, \frac{2}{3}, \frac{3}{4})$	$(\frac{2}{3}, \frac{1}{3}, \frac{1}{4})$
$\Lambda_1$	$(2u, u, 0)$	$(2u, u, 0)$	$(2u', u', 0)$	$(-2u', -u', 0)$	$(2u'', u'', 0)$	$(2u'', u'', 0)$
$\Lambda_2$	$(0, -u, v)$	$(0, -u, -v)$	$(0, -u', v')$	$(0, u', v')$	$(0, -u'', v'')$	$(0, -u'', -v'')$
$\Lambda_3$	$(0, -u, v)$	$(0, u, v)$	$(0, -u', v')$	$(0, -u', -v')$	$(0, -u'', v'')$	$(0, u'', v'')$
$\Lambda_4$	$(2u, u, 0)$	$(-2u, -u, 0)$	$(2u', u', 0)$	$(2u', u', 0)$	$(2u'', u'', 0)$	$(-2u'', -u'', 0)$

sites. We have also observed that the triple cell peaks disappear at high temperatures above  $T_S = 365$  K indicating a structural transition to the ideal undistorted structure, where all Ni sites are identical implying that charge is uniformly distributed on the Ni sites. The low-temperature magnetic diffraction pattern is well explained by a structure of ferromagnetic rows ordered antiferromagnetically, but interestingly with ordered moments present only on the electron-rich Ni sites, which as a consequence of charge disproportionation would have the largest spin moment ( $S = 1$  if  $\text{Ni}^{2+}$ ). The observed magnetic structure on the ordered sites has 2-fold symmetry compared to the 3-fold symmetry of the crystal structure. We have proposed that the magnetic structure could be explained starting from an easy-axis triangular lattice antiferromagnet with additional weak in-plane next-nearest neighbor antiferromagnetic couplings and/or weak ferromagnetic interlayer interactions. Determination of the relative magnitude of the exchanges and anisotropy terms requires measurements of the spin gap and spin-wave dispersion band-width and such measurements are in progress.<sup>27</sup>

Both the magnetic order and structural distortion observed here are very different from the prevailing theoretical model for Jahn-Teller active transition metal ions coupled in a triangular lattice arrangement by near  $90^\circ$  metal-oxygen-metal bonds, which predicts ferro-distortive orbital order and dominant ferromagnetic in-plane interactions,<sup>3</sup> as indeed observed experimentally in  $\text{NaNiO}_2$  (Ref. 10).  $2\text{H-AgNiO}_2$  shows a different type of structural modulation which suggests an alternative mechanism of lifting the large degeneracy in the orbital sector by means of charge ordering, leading to non-equivalent Ni sites, some electron rich and others electron depleted. In the ideal, undistorted crystal structure each Ni site has one electron in the two-fold degenerate  $e_g$  orbital and at the structural transition below  $T_S = 365$  K the lattice separates into two sub-systems. From each hexagon of Ni ions one electron jumps to the Ni site in the center to form an orbitally-nondegenerate  $e_g^2$  state, and this leaves a surrounding honeycombe network of mainly electronically-inactive  $\text{Ni}^{4+}$  sites but with an extra electron for every two sites (most likely itinerant and therefore distributed with equal probability on every site,  $1/8$  filled  $e_g$  orbital on the honeycombe network). Fur-

ther experiments in particular NMR, X-ray absorption (XAFS) or photoelectron spectroscopy (XPS) would be needed to confirm such a scenario and determine quantitatively the extent of the charge disproportionation.

Further studies are also needed to understand better the very different magnetic behaviour of the expanded and contracted Ni sites, attributed in the charge-order scenario to electron-rich and -depleted sites, respectively. Band structure calculations<sup>16</sup> suggest that as a result of charge order the Ni ions in the center of expanded  $\text{NiO}_6$  octahedra become more localized and then the magnetic order at those sites at low temperatures could be understood in terms of stacked triangular lattices with a large spin moment (valence close to  $\text{Ni}^{2+}$  with  $S = 1$ ), whereas the remaining electron-depleted Ni2 and Ni3 sites located inside contracted  $\text{NiO}_6$  octahedra maintain a large itinerant character (due to shorter Ni-O distances and thus stronger orbital overlap with the oxygens); in this scenario the itinerant sites do not show a strong tendency to magnetic order because of insufficiently large density of states at the Fermi level. In fact, the band structure calculations suggested that a small ordered moment of  $\sim 0.1 \mu_B$  may be induced on the contracted Ni3 sites by the ordering of the large Ni1 moments. We note that recent  $\mu\text{SR}$  measurements<sup>24</sup> have reported an anomalous temperature-dependence of the local static magnetic fields which may be due to small ordered moments on the honeycombe Ni sites with a different temperature-dependence compared to the large moments on the Ni1 sublattice.

Another interesting aspect worthwhile looking into is the role of interlayer coupling in stabilizing the magnetic order and structural distortion. It could be investigated by looking at a system in which that coupling could be modified without modifying the intralayer exchange integrals.  $\text{AgNiO}_2$  is a rare example of a delafossite having two polymorphs whose synthesis is feasible<sup>30</sup> and therefore the ideal candidate for further studies seems to be the  $3\text{R-AgNiO}_2$  polytype. The only difference between the latter and the  $2\text{H-AgNiO}_2$  is the way the  $\text{NiO}_2$  layers are stacked on top of each other.

## IX. ACKNOWLEDGEMENTS

We would like to thank I.I. Mazin and M.D. Johannes for collaboration on related work and S.J. Blundell, T. Lancaster, N. Shannon, and R. Moessner for useful discussions. We also thank E. Suard and W. Kockelmann for technical assistance with the experiments at the ILL and ISIS, D. Prabhakaran for help with the SQUID and heat capacity measurements, and the initial stages of sample preparation, and A. El-Turki for performing the SEM/EDX analysis. The research was supported in part by EPSRC U.K. grants EP/C51078X/2 (EW) and GR/R76714/02 (RC), a CASE award from the EPSRC and ILL (EMW), the EU programme at the ILL. The D2B measurements were supported by EPSRC U.K. grant GR/R88601/02.

## APPENDIX A: STRUCTURE FACTORS

Here we list the measured and fitted nuclear (Table V) and magnetic (Table VI) structure factors.

## APPENDIX B: CO-REPRESENTATION ANALYSIS OF THE TRIPLE-CELL CRYSTAL STRUCTURE

Here we look in more detail at the symmetry properties of the experimentally determined supercell modulation and show how the the basis vectors for the charge and displacement order patterns can be used to uniquely identify the distorted space group. Specifically we will find all symmetry operations that leave the order pattern invariant to determine the space group. We follow closely ref. 28 where the basic concepts of co-representation analysis as applied to the symmetry reduction for  $\mathbf{q}$ -vector modulations at a generic point in the Brillouin zone are explained. We first construct from the irreducible representation (*irrep*) modes a new set of modes, known as corepresentation (*corep*) modes, which are invariant upon application of the anti-unitary operator  $KI$ , where  $I$  is the inversion operator ( $h_{13}$  in Kovalev notation) and  $K$  is the complex conjugation. When combined with their complex conjugate, these modes are centrosymmetric even if the propagation vector is not equivalent to its inverse, as it is the case here. In other words, the “corep little group” contains all 24 symmetry operators in  $P6_3/mmc$ . We can then re-write both the scalar and the polar vector modulation as a linear combinations of corep modes, and directly assess their symmetry. It is important to remember that the coefficients of the corep modes are complex-conjugated upon application of an anti-unitary operator.

The irrep-corep matrix for space group 194 and propagation vector  $\mathbf{q}_0 = (1/3, 1/3, 0)$  is listed in Kovalev<sup>29</sup>, and, for irreducible representations  $\tau_1$  and  $\tau_2$  can be summarized as follows:

- Each of the two irreps generates exactly one corep, which has the same matrices as the original irrep on the unitary operators. For this reason, we will still use the notation  $\tau_1$  and  $\tau_2$  to indicate the generated coreps.
- Operators  $h_1, h_3, h_5, h_7, h_9, h_{11}, Kh_{13}, Kh_{15}, Kh_{17}, Kh_{19}, Kh_{21}, Kh_{23}$  : all coefficients are 1 for both  $\tau_1$  and  $\tau_2$
- Operators  $h_{16}, h_{18}, h_{14}, h_{22}, h_{24}, h_{20}, Kh_4, Kh_6, Kh_2, Kh_{10}, Kh_{12}, Kh_8$ : coefficients are 1 for  $\tau_1$  and -1 for  $\tau_2$

The corep modes  $\delta$  can be obtained from the irrep modes  $\tau$  as

$$\delta = \frac{1}{2}(\tau + KI\tau) \quad (B1)$$

### 1. Scalar Modes

Since Ni is on the inversion center, and the mode is scalar and real, we have  $KI\tau = \tau$ , and  $\delta = \tau$ . We can then re-write the scalar modulation in Eq. (1) as

$$\zeta = e^{i\pi/3} \left[ (\delta_1 + \delta_2) + e^{i4\pi/3}(\delta_1 - \delta_2) \right] \quad (B2)$$

### 2. Vector Modes

Here, site permutation, polar vector inversion and complex conjugation all come into play, since

$$\begin{aligned} KI\tau(1) &= -\overline{\tau(2)}e^{i4\pi/3} \\ KI\tau(3) &= -\overline{\tau(4)}e^{i4\pi/3} \end{aligned} \quad (B3)$$

where  $\tau(1)$  is the mode on atom 1 etc. The irrep modes are

$$\begin{aligned} \tau(1) &= \pm\tau(3) = (e^{i\pi/6}, e^{i\pi/2}, 0) \\ \tau(2) &= \pm\tau(4) = (e^{i\pi/2}, e^{i\pi/6}, 0) \end{aligned} \quad (B4)$$

where the + and – are for irrep 1 and 2, respectively (see  $\tau_1$  and  $\tau_2$  in Table III). By inserting eq. (B3) and (B4) into eq. (B1), and after some manipulation, one obtains

$$\delta = \frac{\sqrt{3}}{2}e^{-i\pi/6}\tau \quad (B5)$$

We can then re-write the vector modulation eq. (5) as

$$\xi = \frac{\sqrt{3}}{3}e^{i4\pi/3} \left[ (\delta_1 + \delta_2) + e^{i4\pi/3}(\delta_1 - \delta_2) \right] \quad (B6)$$

### 3. Symmetry analysis

It is now straightforward to perform the symmetry analysis on the scalar and vector modulation. There are four cases, depending on whether the operators are unitary or anti-unitary and whether their matrices have the same or opposite signs for  $\tau_1$  and  $\tau_2$  or  $\tau_1$  and  $\tau_2$ .

**Case 1 :** Unitary, same sign (e.g.,  $h_3$ )

$$h_3\zeta = e^{i\pi/3} [(\delta_1 + \delta_2) + e^{i4\pi/3}(\delta_1 - \delta_2)] = \zeta \quad (\text{B7})$$

$$h_3\xi = \frac{\sqrt{3}}{3} e^{i4\pi/3} [(\delta_1 + \delta_2) + e^{i4\pi/3}(\delta_1 - \delta_2)] = \xi$$

so both modes are invariant.

**Case 2 :** Unitary, opposite sign (e.g.,  $h_{16}$ )

$$h_{16}\zeta = e^{i\pi/3} [(\delta_1 - \delta_2) + e^{i4\pi/3}(\delta_1 + \delta_2)] \neq \zeta \quad (\text{B8})$$

$$h_{16}\xi = \frac{\sqrt{3}}{3} e^{i4\pi/3} [(\delta_1 - \delta_2) + e^{i4\pi/3}(\delta_1 + \delta_2)] \neq \xi$$

so neither mode is invariant.

**Case 3 :** Antiunitary, same sign (e.g.,  $Kh_{13}$ )

$$Kh_{13}\zeta = e^{-i\pi/3} [(\delta_1 + \delta_2) + e^{-i4\pi/3}(\delta_1 - \delta_2)] \neq \zeta \quad (\text{B9})$$

$$Kh_{13}\xi = \frac{\sqrt{3}}{3} e^{-i4\pi/3} [(\delta_1 + \delta_2) + e^{-i4\pi/3}(\delta_1 - \delta_2)] \neq \xi$$

so neither mode is invariant.

**Case 4 :** Antiunitary, opposite sign (e.g.,  $Kh_6$ )

$$Kh_6\zeta = e^{-i\pi/3} [(\delta_1 - \delta_2) + e^{-i4\pi/3}(\delta_1 + \delta_2)] \quad (\text{B10})$$

$$= e^{-i5\pi/3}(\delta_1 + \delta_2) + e^{-i\pi/3}(\delta_1 - \delta_2)$$

$$= e^{i\pi/3}(\delta_1 + \delta_2) + e^{i5\pi/3}(\delta_1 - \delta_2) = \zeta$$

$$Kh_6\xi = \frac{\sqrt{3}}{3} e^{-i4\pi/3} [(\delta_1 - \delta_2) + e^{-i4\pi/3}(\delta_1 + \delta_2)]$$

$$= \frac{\sqrt{3}}{3} [e^{-i2\pi/3}(\delta_1 + \delta_2) + e^{-i4\pi/3}(\delta_1 - \delta_2)]$$

$$= \frac{\sqrt{3}}{3} [e^{i4\pi/3}(\delta_1 + \delta_2) + e^{i2\pi/3}(\delta_1 - \delta_2)] = \xi$$

so both modes are invariant.

In summary, both modes are invariant upon application of the operators  $h_1, h_3, h_5, h_7, h_9, h_{11}, Kh_4, Kh_6, Kh_2, Kh_{10}, Kh_{12}, Kh_8$  and the resulting modulated structure is invariant by the same operators *without* the complex conjugation. These operators represent all the *proper* rotations of space group  $P6_3/mmc$  - in other words, the six-fold screw axis and the associated orthogonal 2-fold axes. Taking into account the loss of translational symmetry due to the propagation vector, the resulting space group is  $P6_322$  with the unit cell of dimensions  $\sqrt{3}a_0 \times \sqrt{3}a_0 \times c$ .

<sup>1</sup> For a review see G. Misguich and C. Lhuillier in *Frustrated spin systems*, edited by H. T. Diep, (World-Scientific, Singapore, 2003), p.229.

<sup>2</sup> For a review see A. Harrison, J. Phys.: Condens. Matter **16** S553 (2004).

<sup>3</sup> M. V. Mostovoy and D. I. Khomskii, Phys. Rev. Lett. **89**, 227203 (2002).

<sup>4</sup> S. Nakatsuji, Y. Nambu, H. Tonomura, O. Sakai, S. Jonas, C. Broholm, H. Tsunetsugu, Y. Qiu, Y. Maeno, Science **309**, 1697 (2005).

<sup>5</sup> F. Vernay, K. Penc, P. Fazekas, F. Mila, Phys. Rev. B **70**, 014428 (2004).

<sup>6</sup> Y.J. Shin, J.P. Doumerc, P. Dordor, C. Delmas, M. Pouchard, P. Hagenmuller, J. Solid State Chem. **107**, 303 (1993).

<sup>7</sup> A. J. W. Reitsma, L. F. Feiner, and A. M. Oleś, New J. Phys. **7** 121 (2005); A.-M. Daré, R. Hayn and J.-L. Richard, Europhys. Lett. **61**, 803 (2003).

<sup>8</sup> J.-H. Chung, Th. Proffen, S. Shamoto, A.M. Ghorayeb, L. Croguennec, W. Tian, B.C. Sales, R. Jin, D. Mandrus, T. Egami, Phys. Rev. B **71**, 064410 (2005) and references therein.

<sup>9</sup> S. J. Clarke, A. J. Fowkes, A. Harrison, R. M. Ibberson, and M. J. Rosseinsky, Chem. Mater. **10**, 372 (1998).

<sup>10</sup> E. Chappel, M. D. Núñez-Regueiro, G. Chouteau, O. Is-

nard, and C. Darie, Eur. Phys. J. B **17**, 615 (2000); M. Sofin, and M. Jansen, Z. Naturforsch. **B60**, 701-704 (2005) and references therein.

<sup>11</sup> M. Schreyer and M. Jansen, Angew. Chem. **41**, 643 (2002); H. Yoshida, Y. Muraoka, T. Sörgel, M. Jansen, and Z. Hiroi, Phys. Rev. B **73**, 020408(R) (2006); J. Sugiyama, Y. Ikeda, K. Mukai, J. H. Brewer, E. J. Ansaldo, G. D. Morris, K. H. Chow, H. Yoshida, and Z. Hiroi, Phys. Rev. B **73**, 224437 (2006); U. Wedig, P. Adler, J. Nuss, H. Modrow, and M. Jansen, Solid State Sci. **8**, 753-763 (2006);

<sup>12</sup> T. Sörgel, M. Jansen, J. Solid State Chem., **180**, 8 (2007).

<sup>13</sup> M. D. Johannes, S. Streltsov, I. I. Mazin, D. I. Khomskii, Phys. Rev. B **75**, 180404(R) (2007).

<sup>14</sup> A. Wichainchai, P. Dordor, J. P. Doumerc, E. Marques-taut, Mi. Pouchard, P. Hagenmuller, A. Ammar, J. Solid State Chem. **74**, 126 (1988).

<sup>15</sup> T. Sörgel and M. Jansen, Z. Anorg. Allg. Chem. **631**, 2970 (2005).

<sup>16</sup> E. Wawrzyńska, R. Coldea, E.M. Wheeler, I.I. Mazin, M.D. Johannes, T. Sörgel, M. Jansen, R.M. Ibberson, and P.G. Radaelli, Phys. Rev. Lett. **99**, 157204 (2007).

<sup>17</sup> J. Rodriguez-Carvajal, Physica B **192**, 55 (1993).

<sup>18</sup> K. Nakahigashi, Y. Shimomura, N. Fukuoka, Acta Crystallographica A **28**, 234 (1972); D. Rodic, V. Spasojevic, V. Kusigerski, R. Tellgren, H. Rundlof, Physica Status Solidi

- B **218**, 527 (2000); P. E. Tomaszewski, *Phase Transitions* **38**, 127 (1992).
- <sup>19</sup> J. M. Tarascon, G. Vaughan, Y. Chabre, L. Seguin, M. Anne, P. Strobel, G. Amatucci, *Journal of Solid State Chemistry* **147**, 410 (1999); A. Hirano, R. Kanno, Y. Kawamoto, Y. Takeda, K. Yamaura, M. Takano, K. Ohyama, M. Ohashi, Y. Yamaguchi, *Solid State Ionics* **78**, 123 (1995).
- <sup>20</sup> I. D. Brown, in *Structure and Bonding in Crystals*, edited by M. O'Keefe and A. Navrotsky (Academic Press, New York, 1981), Vol. **2**, pp. 130; N. E. Brese et al., *Acta Crystallogr. Sect. B* **47**, 192 (1991).
- <sup>21</sup> J.A. Alonso, J.L. García-Muñoz, M.T. Fernández-Díaz, M.A.G. Aranda, M.J. Martínez-Lope, M.T. Casais, *Phys. Rev. Lett.* **82**, 3871 (1999).
- <sup>22</sup> W. Sikora, F. Białas, and L. Pytlik, *J. Appl. Cryst.* **37**, 1015 (2004).
- <sup>23</sup> M. Bejas, A. Greco, A. Foussats, *Phys. Rev. B* **75**, 033101 (2007).
- <sup>24</sup> T. Lancaster, S. J. Blundell, P. J. Baker, M. L. Brooks, W. Hayes, F. L. Pratt, R. Coldea, T. Soergel, M. Jansen, *Phys. Rev. Lett.* **100**, 017206 (2008).
- <sup>25</sup> A. V. Chubukov and Th. Jolicoeur, *Phys. Rev. B* **46**, 11137 (1992); Th. Jolicoeur, E. Dagotto, E. Gagliano, and S. Bacci, *Phys. Rev. B* **42**, 4800 (1990).
- <sup>26</sup> P. A. Slotte and P. C. Hemmer, *J. Phys. C: Solid State Phys.* **17**, 4645 (1984).
- <sup>27</sup> E. M. Wheeler *et al.* (in preparation).
- <sup>28</sup> P. G. Radaelli and L. C. Chapon, *Phys. Rev. B* **76**, 054428 (2007).
- <sup>29</sup> O. V. Kovalev, "Irreducible representations, Induced Representations and Corepresentations", 2nd edition, Ed. Harold T. Stokes and Dorian M. Hatch, Gordon and Breach Science Publishers, 1993, page 251.
- <sup>30</sup> X. X. Liu, C. P. M. Oberndorfer and M. Jansen, *J. Electrochem. Soc.* **155**, E1 (2008).

TABLE V: List of supercell structural peaks associated with the tripling of the unit cell in the basal plane with the observed and calculated unit cell structure factors for the model of expanded and contracted Ni-O bonds shown in Fig. 4. The observed  $|F|^2$  is the peak intensity corrected for instrumental resolution effects, divided by the peak multiplicity and normalized per unit cell of the  $P6_322$  group. For completeness a selection of the nominal peaks of the ideal structure ( $P6_3/mmc$  space group) is also given, and the peak indices are given in both space groups.

	$Q$ ( $\text{\AA}^{-1}$ )	$(h, k, l)$ $P6_322$	$(h, k, l)$ $P6_3/mmc$	observed $ F $ ( $10^{-14}$ m)	calculated $ F $ ( $10^{-14}$ m)
nominal peaks	1.026	002	002	6.24	6.36
	2.052	004	004	7.19	6.76
	2.469	110	100	1.14	0.94
	2.523	111	101	5.89	5.98
	2.675	112	102	5.86	6.12
	2.911	113	103	2.79	2.90
	3.080	006	006	4.49	4.30
	3.212	114	104	5.83	5.92
	3.562	115	105	6.40	6.52
	3.947	116	106	11.36	11.40
	4.105	008	008	5.69	5.43
	4.278	300	110	18.07	16.55
	4.359	117	107	5.34	5.40
	supercell peaks	1.425	010	2/3 -1/3 0	0.15
1.515		011	2/3 -1/3 1	0.24	0.24
1.756		012	2/3 -1/3 2	0.05	0.09
2.097		013	2/3 -1/3 3	0.02	0.02
2.851		020	4/3 -2/3 0	0.31	0.35
2.898		021	4/3 -2/3 1	0.57	0.53
2.936		015	2/3 -1/3 5	0.23	0.23
3.031		022	4/3 -2/3 2	0.14	0.19
3.393		016	2/3 -1/3 6	0.00	0.16
3.514		024	4/3 -2/3 4	0.00	0.15
3.807		211	4/3 1/3 1	0.35	0.22
3.836		025	4/3 -2/3 5	0.53	0.50
3.865		017	2/3 -1/3 7	0.46	0.26
3.910		212	4/3 1/3 2	0.60	0.62
4.074		213	4/3 1/3 3	0.37	0.42
4.105		026	4/3 -2/3 6	0.39	0.35
4.295		214	4/3 1/3 4	0.73	0.66
4.562		215	4/3 1/3 5	0.30	0.26
4.586		027	4/3 -2/3 7	0.49	0.56
4.998		028	4/3 -2/3 8	0.35	0.22
5.166		311	5/3 2/3 1	0.67	0.67
5.209		217	4/3 1/3 7	0.37	0.19
5.242		312	5/3 2/3 2	0.71	0.74
5.366		313	5/3 2/3 3	0.56	0.48
5.535		314	5/3 2/3 4	0.77	0.77
5.575		218	4/3 1/3 8	0.63	0.58
5.703		040	8/3 -4/3 0	0.54	0.60
5.726		041	8/3 -4/3 1	0.89	0.90
5.745	315	5/3 2/3 5	0.56	0.65	
5.794	042	8/3 -4/3 2	0.41	0.32	
5.821	0 1 11	2/3 -1/3 11	0.22	0.21	
5.870	0 2 10	4/3 -2/3 10	0.17	0.12	

TABLE VI: List of magnetic Bragg peaks with the observed and calculated unit cell structure factors for the magnetic structure in Fig. 10. The observed  $|F|^2$  is the peak intensity corrected for instrumental resolution effects, divided by the peak multiplicity and normalized per unit cell of the  $P6_322$  group. For completeness the peak indices are given both in the distorted ( $P6_322$ ) and the ideal ( $P6_3/mmc$ ) crystal structures.

$Q$ ( $\text{\AA}^{-1}$ )	$(h, k, l)$ $P6_322$	$(h, k, l)$ $P6_3/mmc$	observed $ F $ ( $10^{-14}$ m)	calculated $ F $ ( $10^{-14}$ m)
0.714	1/2 0 0	1/6 1/6 0	0.61	0.71
0.879	1/2 0 1	1/6 1/6 1	0.28	0.33
1.236	1/2 -1 0	1/2 0 0	0.00	0.00
1.250	1/2 0 2	1/6 1/6 2	0.37	0.39
1.339	1/2 -1 1	1/2 0 1	0.74	0.72
1.607	1/2 -1 2	1/2 0 2	0.00	0.00
1.697	1/2 0 3	1/6 1/6 3	0.16	0.16
1.889	1/2 1 0	-1/6 5/6 0	0.58	0.63
1.957	1/2 1 1	1/6 5/6 1	0.34	0.35
1.957	3/2 -1 1	1/6 5/6 1	0.34	0.35
1.974	1/2 -1 3	1/2 0 3	0.48	0.45
2.142	3/2 0 0	1/2 -1 0	0.00	0.00
2.150	1/2 1 2	1/6 5/6 2	0.50	0.53
2.150	3/2 -1 2	1/6 5/6 2	0.50	0.53
2.173	1/2 0 4	1/6 1/6 4	0.15	0.20
2.202	3/2 0 1	1/2 -1 1	0.70	0.68